https://doi.org/10.1038/s41566-023-01204-1

A double-tapered fibre array for pixel-dense gamma-ray imaging

Luying Yi [1,6], **Bo Hou** [1,6], **He Zhao** [1,2], **Hong Qi Tan** [3] & **Xiaogang Liu** [1,2,4,5] ✉

Luminescence intensity in photodetectors, radiation imagers and light-emitting diodes is proportional to the thickness of the light-emitting layer. However, a thick emitting layer reduces light output because of incoherent photon scattering and attenuation. Here we present the design of double-tapered optical-fibre arrays that can drastically increase the light output of thick light-emitting layers by progressively filling more propagation modes along the fibre's depth. To enhance the light-collection efficiency and imaging resolution, the upper taper angle of each fibre is greater than the lower angle. By filling the fibre substrate with perovskite nanocrystals from a scale of micrometres thick to centimetres thick, large-scale pixel-dense X-ray or gamma-ray detector arrays can be fabricated. We demonstrate X-ray imaging with a spatial resolution of 22 lp mm^{-1}. Pixelated gamma-ray imaging is also demonstrated using a nanocrystal scintillator film with a thickness of 4 mm and ~10,000 pixels under focused 6-MeV irradiation. Dynamic changes in the energy spectrum (5 keV to 10 MeV) and dose rate (3.5 nGy s^{-1} to 96 mGy s^{-1}) can be conveniently monitored using a hemispherical fibre array dosimeter with a field of view of 150°. This study presents a high-throughput approach for fabricating thick emitter layers that could be applied to biomolecular or mechanical force sensing, medical imaging and ion beam therapy.

Experimental nuclear physics uses gamma-ray detection to perform analyses of nuclear fuel cycles and nuclear power plants, as well as to detect and monitor environmental conditions. Such gamma-ray detection is also used for a range of societally relevant applications, such as diagnostic imaging, oncology, homeland security and high-energy astronomy[1–3]. In spite of advances in scintillator fabrication and photodetectors, large-area high-sensitivity gamma-ray imaging still remains a formidable challenge[4–6]. This is because it is challenging and expensive to fabricate high-sensitivity detector arrays with dense pixels over large areas, such as photomultiplier tube arrays or multi-pixel photon counters, which are necessary to compensate for weak scintillation output and insufficient radiation absorption. Perovskite semiconductors or

scintillators have recently been investigated for high-energy beam detection because of their large stopping power, excellent charge carrier collection and high energy conversion efficiency[7–15]. It has been demonstrated that single-crystalline or hybrid perovskite-based photoconductors can detect gamma rays, especially via gamma-ray spectroscopy, with impressive energy resolution. However, the fabrication of large-scale pixelated array sensors based on perovskite semiconductors for gamma-ray imaging is rather difficult and costly due to the difficulty in growing large and high-quality single crystals and the requirement for expensive, specialized detector arrays for the conversion of radiation into electric signals[1,16–18]. In recent years, perovskite nanoscintillators have been integrated directly into charge-coupled

[1]Department of Chemistry, National University of Singapore, Singapore, Singapore. [2]Joint School of National University of Singapore and Tianjin University, International Campus of Tianjin University, Binhai New City, Fuzhou, China. [3]Division of Radiation Oncology National Cancer Centre Singapore, Singapore, Singapore. [4]Center for Functional Materials, National University of Singapore Suzhou Research Institute, Suzhou, China. [5]Institute of Materials Research and Engineering, Agency for Science, Technology and Research, Singapore, Singapore. [6]These authors contributed equally: Luying Yi, Bo Hou. ✉e-mail: chmlx@nus.edu.sg
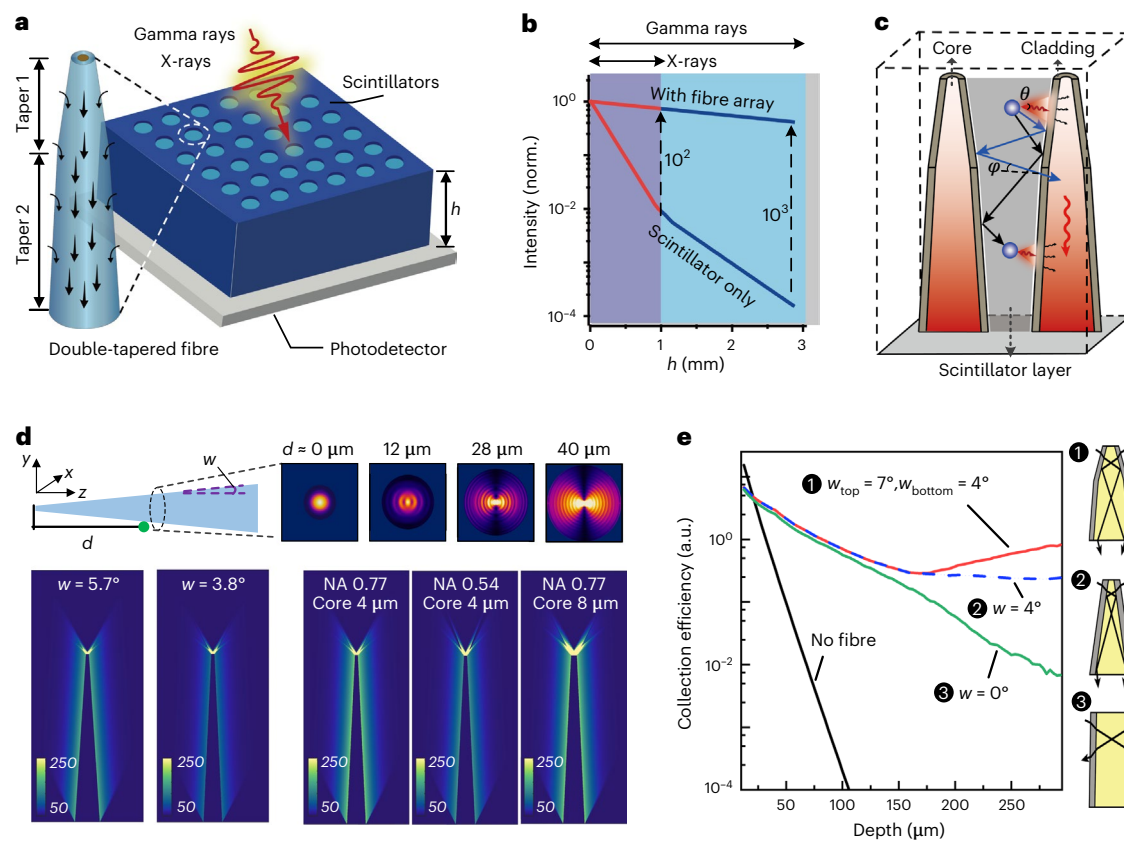
Fig. 1 | Structural properties of transparent double-tapered optical-fibre arrays for directional light collection. a, Schematic of scintillator-enclosed fibre arrays for X-ray and gamma-ray detection and imaging. In the fibre array, radioluminescence can travel several centimetres. The radioluminescence will be exhausted and undetectable in the absence of the fibre array due to the absorption and scattering of the scintillator layer. **b**, Comparison of optical energy losses in scintillator layers with and without the fibre array. Red and blue lines denote the optical energy loss for X-rays and gamma rays, respectively. norm., normalized. **c**, Schematic luminescence propagation path affected by photon recycling in scintillators. The luminescence enters the fibre array primarily in three ways: (1) photons emitted within the escape-cone angle θ directly enter the transparent fibre (red arrow); (2) after photons in the scintillator film are reflected several times, their incidence angle φ falls back to

the escape-cone angle and they enter transparent fibres (blue arrow); (3) photons are reabsorbed and re-emitted isotropically during propagation, while those photons that fall within the escape-cone angle enter transparent fibres (black arrow). **d**, Top panel: electric-field patterns of the tapered fibre at different depths, showing that a larger diameter can support higher-order propagating modes. Bottom panel: analytically calculated collection fields for different taper angles w, NAs and core diameters. The numbers on colour bars represent the amplitude of collection efficiency. **e**, Simulation of luminescence collecting efficiency with no fibre array, cylindrical fibre arrays, tapered fibre arrays and double-tapered fibre arrays. CsPbBr$_3$ nanocrystals are used as the luminescent materials in the simulations, and their optical parameters are shown in Supplementary Fig. 1. a.u., arbitrary units.

---

devices to achieve X-ray imaging[19–22]. However, for gamma rays to be effectively absorbed, the perovskite scintillator layer must be several millimetres to centimetres thick (Supplementary Fig. 1)[1,23,24]. Light penetration and spatial resolution would be limited with millimetre-thick perovskite scintillators due to lateral photon scattering and inherent self-absorption.

Optical fibres can enhance light coupling, perform optical signal transport and enable photonic integrated circuits with low-loss interfaces[25–29]. Moreover, theoretical studies suggest that tapered or double-tapered optical fibres can act as high-power amplifiers by facilitating the propagation of evanescent waves on fundamental modes in the tapered region[30]. In this Article, we extend theoretical analysis and experimentally validate the possibility of achieving high-sensitivity gamma-ray imaging using a flexible, double-tapered fibre array and perovskite nanocrystal scintillators. The nanocrystal scintillators are solution-processed and spin-coated onto a fibre-array substrate that is fabricated using a three-dimensionally (3D) printed mould (Fig. 1a). Notably, a double-tapered optical fibre with low attenuation can guide scintillator emission over a distance of more than 5 cm with less than 50% attenuation (Supplementary Fig. 1). When excited with X-rays

(50 keV), a double-tapered fibre array with a 1-mm-thick scintillator layer showed two orders of magnitude higher luminescence, whereas the fibre array with a 3-mm scintillator layer increased the luminescence intensity by three orders of magnitude upon irradiation with gamma rays (10 MeV; Fig. 1b).

Double-tapered optical fibres are composed of a core and cladding, with refractive indices of n_1 and n_2, respectively. The scintillator layer between two double-tapered fibres forms an inverted tapered structure with a refractive index of n_3. The scintillators emit isotropic light after irradiation. The emitted light incident on the cladding at an incident angle in the escape-cone angle θ, which is greater than θ_1 (arcsin(n_1/n_3sin(arcsin(n_2/n_1) − 2w))) and less than θ_2(arcsin(n_2/n_3)), enters the tapered fibre and propagates in the form of total internal reflection, where w is the taper angle of the fibre (Fig. 1c and Supplementary Fig. 2). Radiation photons not contained in the escape-cone θ are trapped in the scintillator layer. In our design, trapped photons can re-enter the transparent tapered fibre through two main processes in addition to scattering. First, because the light-emitting layer is an inverted tapered structure, the incident angle φ at the cladding interface of trapped photons gradually decreases, causing them to fall
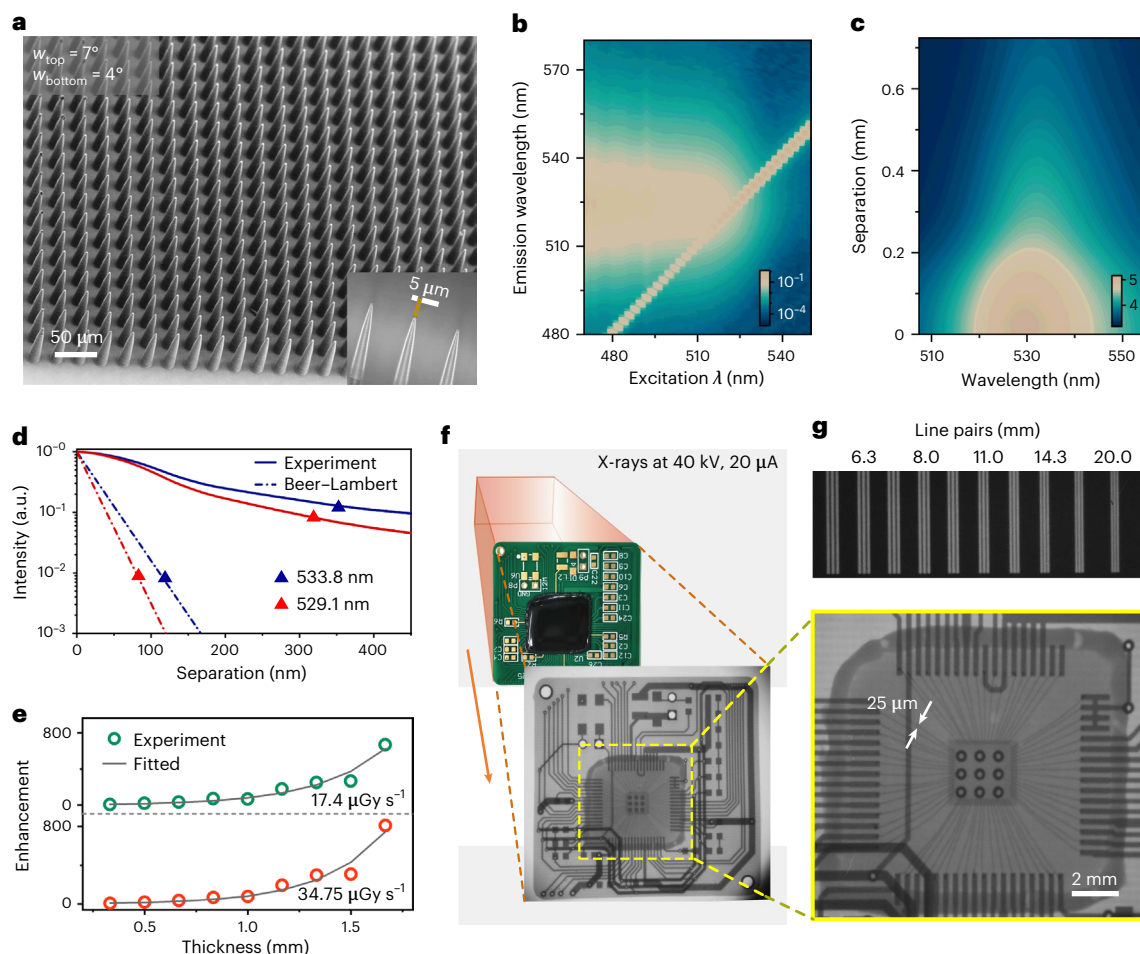
Fig. 2 | Optical characterizations of the double-tapered optical-fibre array for photon recycling and high-resolution X-ray imaging. a, Scanning electron microscopy imaging of a typical double-tapered fibre array. The inserted optical image shows that the fibres have an upper taper angle of 7°, a lower taper angle of 4°, a base diameter of 20 μm and a height of 120 μm. **b**, Measured normalized luminescence spectra as a function of excitation wavelength. The peak position of the emission spectrum is independent of the wavelength of the excitation light. The bright line represents the spectrum of the excitation light. **c**, Light emission map measured experimentally for different separation distances between excitation and collection. The numbers on colour bars in **b** and **c** represent light intensity (a.u., aribitrary units). **d**, Comparison of the observed (solid lines) and expected (dashed lines) decays at 529.1 nm and 533.8 nm based on the Beer–Lambert equation. **e**, Scintillator film enhancement factor versus film thickness under X-ray excitation at two different dose rates. **f**, X-ray imaging of integrated circuits on a printed circuit board using the fibre-array-enclosed scintillator film (voltage, 40 kV; current, 20 μA). **g**, X-ray imaging of standard test patterns for measuring the resolution.

back into the range of escape angle θ and re-enter the tapered fibre. In addition, the trapped photons are reabsorbed by the perovskite scintillators and isotropically re-emitted, which facilitates light collection by randomizing the propagation direction of the photons and redirecting them from the trapped mode to the outcoupling mode of the fibre[31,32]. Although reabsorption is considered a loss mechanism in many applications, the repetitive reabsorption and re-emission (photon recycling) of the photons trapped in the gaps can enhance light extraction within the tapered optical fibre.

We next characterized the light collection properties and optimized the geometry of the tapered optical fibre to maximize the light-collection efficiency and transmission efficiency. We first calculated the light-collection field of the tapered fibre based on the geometrical optics (Supplementary Figs. 3–5). The optical active surface of a tapered fibre extends along its waveguide axis, enabling relatively uniform light collection along the taper (Fig. 1d). This results from the fact that the number of guided modes increases as the diameter of the tapered fibre increases, allowing propagation modes to be progressively populated[33,34]. In contrast, a cylinder fibre can only collect luminescence from the fibre's facet. We compared the collection fields for fibres with different taper angles w, numerical apertures (NAs) and core diameters. We found that the light-collection efficiency increases with increasing fibre NA and w, and the efficiency at the fibre facet increases with the core diameter. With the upper part of the scintillator layer absorbing more excitation photons and the lower end of the fibre determining the spatial resolution of the imaging, the fibre was designed as a double-tapered fibre with an upper taper angle of 7° and a lower taper angle of 4°. Compared with a perovskite layer without fibre arrays, a layer with embedded double-tapered fibre arrays is capable of increasing the light output by over four orders of magnitude (Fig. 1e). For X-rays with different energies, the filling rate of tapered optical fibres and the thickness of the scintillator film must be optimally designed by theoretical analyses (Supplementary Fig. 4).

To prove the concept, we benchmarked the collection performance of the microstructured optical-fibre arrays in perovskite nanocrystals. The optical fibres are made of epoxy resin (refractive index $n_1 = 1.52$) demoulded from a 3D-printed mould and clad with polydimethylsiloxane (PDMS, refractive index $n_2 = 1.41$) elastomer (Fig. 2a). Perovskite nanocrystals act as scintillators (refractive index $n_3 = 1.82$). The perovskite nanocrystals were characterized by measuring their
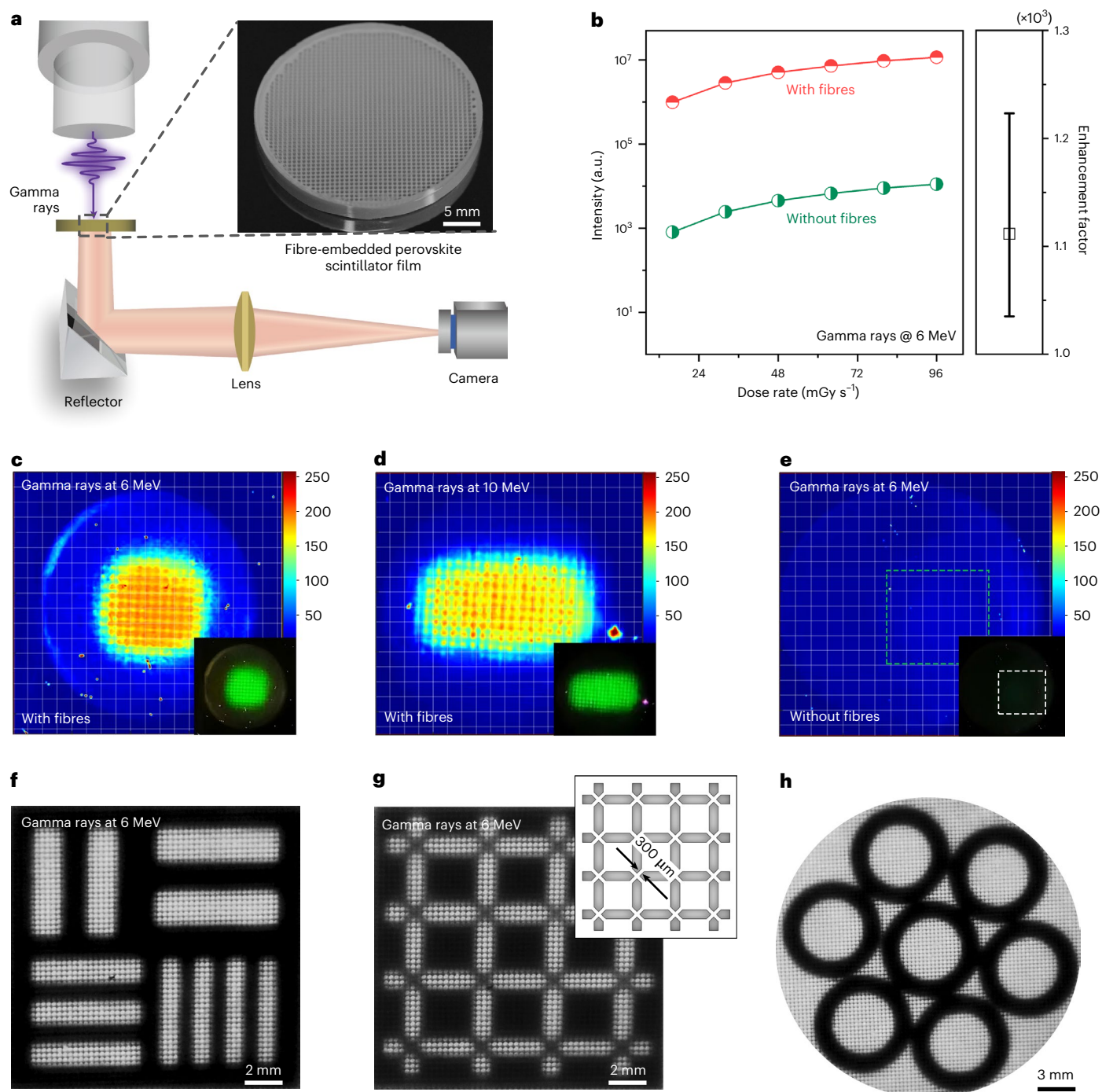
Fig. 3 | Gamma-ray imaging using a fibre-embedded perovskite scintillator film. a, Schematic of the experimental set-up used for real-time gamma-ray imaging. A scintillator film with the fibres is placed between a gamma-ray source and a camera for gamma-ray imaging. **b**, Scintillator film enhancement factor with and without the fibre array, under gamma-ray irradiation at different dose rates. Curves are obtained by integrating all wavelengths and measuring multiple times. The dose rate was measured 15 times with a 30-s interval between each measurement. The error bar represents the standard error of the mean (s.e.m.). **c,d**, Direct imaging of 6-MeV (**c**) and 10-MeV (**d**) gamma rays, using the fibre-embedded scintillator film. **e**, Control imaging of 6-MeV gamma rays without the fibres. The numbers on colour bars in **c**–**e** represent light intensity (a.u., arbitrary units). **f**–**h**, Images of tungsten stencils captured under 6-MeV irradiation. To obtain sufficient image contrast, several tungsten stencils are stacked on top of each other.

excitation spectrum, which represents the relative luminescence intensity as a function of wavelength. Perovskite scintillators exhibited relatively small Stokes shifts and a high quantum yield, leading to the substantial reabsorption of emitted photons (Fig. 2b).

We next investigated the important role of photon recycling in perovskite nanocrystals[32,35–38]. A 20-μm-thick perovskite nanocrystal layer on a PDMS film (100 μm thick) was used to study photon recycling in perovskite nanocrystals without any fibres (Supplementary Fig. 6). We measured the luminescence distributions using an optical microscope (spatial resolution of ~1.5 μm) with independently controlled excitation and collection objectives. At a distance of 600 μm from the excitation point, short-wavelength light is still collectable (Fig. 2c,d), at which the redshift in the emission spectrum relative to the direct emission spectrum (without reabsorption and scattering) is smaller than in the
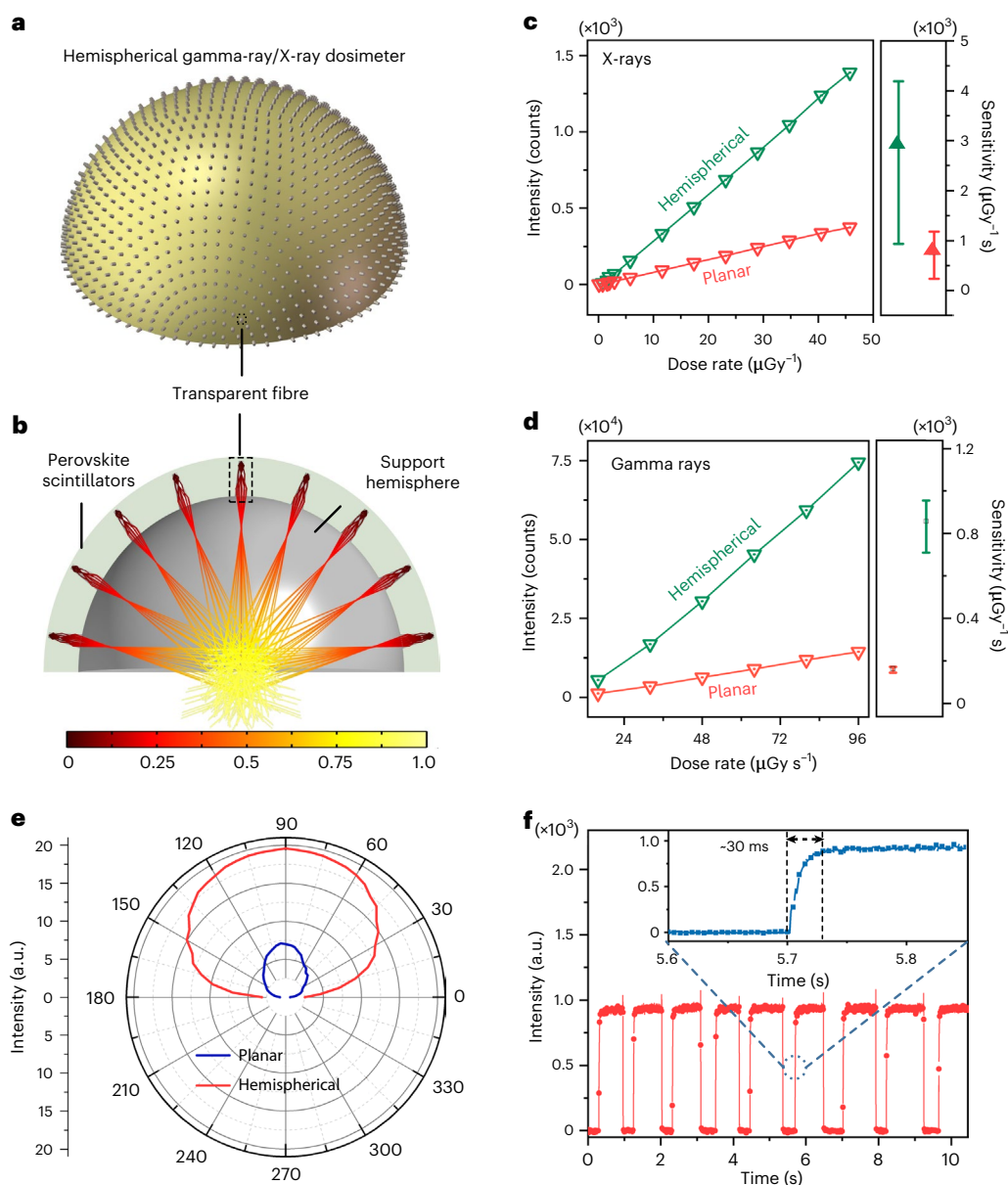
Fig. 4 | Hemispherical dosimeters for X-ray and gamma-ray detection with improved sensitivity and a wider field of view. a, Schematic of a hemispherical dosimeter comprising a flexible base film that connects the fibre array to gap-filled perovskite scintillators, which are mounted on the transparent hemispherical support. **b**, Simulation of light-propagation paths in the hemispherical dosimeter. The numbers on colour bars represent normalized light intensity (a.u., arbitrary units). **c**, Radioluminescence intensity of hemispherical and planar dosimeters versus X-ray dose rate. The detection sensitivity is derived by solving the slope distribution of the curve. Curves are obtained by integrating all wavelengths and measuring multiple times. Each dose rate was measured 15 times. **d**, Radioluminescence intensity of hemispherical and planar dosimeters versus gamma-ray dose rate. Each dose rate was measured 15 times. Data in **c** and **d** are presented as mean values ± standard error of the mean (s.e.m.). **e**, Output signal of hemispherical and planar dosimeters versus the X-ray irradiation direction, indicating that the hemispherical dosimeter has a larger field of view than its planar counterpart. **f**, Dynamic and stability tests of the hemispherical dosimeter. The 30-ms delay is the turn-on time of the thermionic emission-based mini-X-ray tube (P_{max} = 4 W, V_{max} = 50 kV, I_{max} = 79 μA).

purely scattered signal (without re-emission) (Supplementary Fig. 6). This indicates that the emission at a distance of 600 μm is a superposition of the scattered signal and its induced re-emission, demonstrating photon recycling in synthetic perovskite scintillators[32]. Recurring photon recycling in tapered optical fibres improves the light collection efficiency, as calculated by integrating recursive photon recycling processes and simulated by Monte Carlo methods. The microstructured optical fibre can collect and transmit more than 45% of the emitted light at all wavelengths when the internal quantum efficiency of the perovskite is 95% (Methods). Experiments with perovskite nanocrystal layers of different thicknesses revealed that when thicker than 1.75 mm,

the light-collection efficiency increases by approximately three orders of magnitude (Fig. 2e).

In a further set of experiments, double-tapered optical-fibre arrays with embedded perovskite nanocrystals were tested in terms of their sensitivity and spatial resolution for X-ray imaging (Supplementary Fig. 7). Under X-ray excitation, the fibres exhibited substantial light enhancement compared to scintillator-only regions. A 150-μm-thick scintillator film with ~2,000 × 2,000 double-tapered fibres (base diameter of 12 μm) and a light yield of 48,500 photons MeV^{-1} was used to obtain high-quality X-ray images of a standard X-ray test-pattern plate and an integrated circuit chip wire-bonded to a printed circuit board
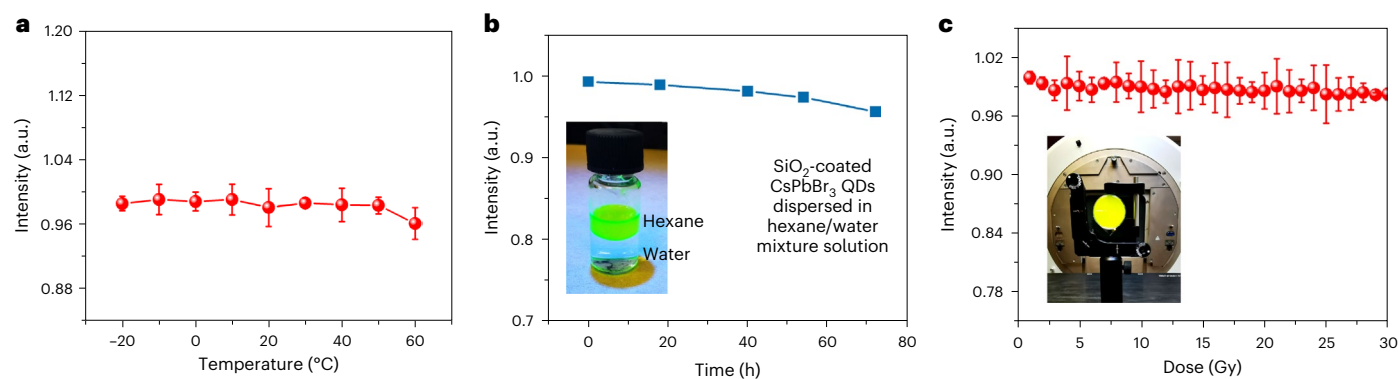
Fig. 5 | Stability tests of scintillator films with embedded optical-fibre arrays. **a**, Thermal stability test of the $CsPbBr_3$ film. The scintillator film was excited ten times with X-rays (voltage, 40 kV; current, 20 μA) at each temperature. **b**, Emission intensity of $CsPbBr_3$ quantum dots (QDs) dispersed in water versus time. **c**, Radioluminescence under gamma-ray irradiation with 10-MeV maximum energy and ~0.1 Gy s^{-1} dose rate. The irradiance stability experiment was repeated ten times. Data in **a** and **b** are presented as mean values ± standard error of the mean (s.e.m.). a.u., arbitrary units.

(Fig. 2f,g), clearly revealing bond wires of 25 μm in width. Specifically, the spatial resolution, defined as the spatial frequency value at a modulation transfer function (MTF) of 0.2, was ~22 line pairs (lp) per millimetre for a 150-μm-thick film. A 0.8-mm-thick film with the fibre array still achieved a spatial resolution of 5 lp mm^{-1}, which is much higher than the film without the fibre array (~1 lp mm^{-1}; Supplementary Figs. 8 and 9). Our mechanistic investigations indicate that tapered fibres greatly reduce light scattering to the surroundings, and the increase in output light improves the imaging contrast, which results in images with a better MTF (Supplementary Fig. 10). This mechanism is also applicable to other scintillators, such as gadolinium oxysulfide (Supplementary Fig. 8).

In addition to their ability to detect X-rays, perovskite scintillators also possess high gamma-ray absorption[19]. Given that scintillator emission can be propagated several centimetres by our transparent fibre arrays, we anticipate that the system can perform well in gamma-ray detection. To validate this hypothesis, we constructed a 4-mm-thick scintillator film embedded with double-tapered fibre arrays to image the high-energy gamma-ray spot patterns used in clinical medicine and to detect their dose (Fig. 3a). When irradiated at various dose rates with 6-MeV irradiation (peak energy of 1 MeV), the embedded scintillator film exhibited an output signal more than 1,000 times higher than a pure perovskite film (Fig. 3b). Embedded scintillator films also allowed visualization of the spot shapes of gamma-ray sources at 6 MeV and 10 MeV (peak energy of 2 MeV), which was not feasible with pure perovskite films (Fig. 3c–e and Supplementary Video 1). To achieve pixel-dense, large-area gamma-ray imaging, we also fabricated a 4-mm-thick scintillator film with ~10,000 double-tapered fibres (base diameter of 250 μm). Customized tungsten stencils were clearly imaged under 6-MeV irradiation, and structures with a size of 300 μm could be distinguished (Fig. 3f–h). Although the fibre diameter can be further reduced, Compton and photon scattering is likely to lower the resolution of megaelectronvolt gamma-ray imaging. Furthermore, gamma-ray spectroscopy has been performed using $CsPbBr_3$ scintillator films containing tapered fibre arrays. A spectral resolution of 8.9% was obtained, compared with 27% of reported liquid scintillators loaded with $CsPbBr_3$ quantum dots (Supplementary Fig. 11)[39].

A fibre-array-containing thin film can be readily modified into a hemispherical dome, enabling a dosimeter to detect radiation more accurately and view radiation from a wider angle (Fig. 4a). The basic design consists of a flexible substrate and an ~400 double-tapered fibre array with a diameter of 400 μm and a height of 3 mm. Once the fibre voids are filled with $CsPbBr_3$ nanocrystals, the flexible substrate is wrapped around a transparent hemisphere. The double-tapered fibre array can concentrate scintillator emission at the centre of the hemisphere due to its spatial confinement and collimating effect (Fig. 4b). Radiation sources perpendicular to the hemispherical detector resulted in a 3.9-fold and 5.4-fold higher detection sensitivity for X-rays and gamma rays, respectively, than fibre-enclosed planar detectors (Fig. 4c,d). The detection limits for X-rays (3.5 nGy s^{-1}) and gamma rays (21.8 μGy s^{-1}) were determined by measuring the dark noise signal and the sensitivity derived from the slope of fitting lines (Supplementary Fig. 12)[40]. In addition, the hemispherical detector maintained a highly consistent detection performance for incident gamma rays over the entire 150° viewing angle range (Fig. 4e). The transient output signal of the hemispherical detector has good repeatability, and the 30-ms delay is the turn-on time of the thermionic emission-based X-ray source (Fig. 4f). The measured photoluminescence lifetime of the scintillator film with embedded optical fibres is 21 ns. In the temperature range of −20–60 °C and under 30-Gy radiation, the scintillator film has less than 4% change in radioluminescence intensity (Fig. 5a–c and Supplementary Fig. 11).

A key feature of our double-tapered optical-fibre array system is its applicability in all situations where luminescence penetration depth is insufficient, such as near-infrared detectors with upconversion materials, X-ray or gamma-ray detectors with perovskite scintillators, and electrically excited light-emitting diodes[41]. By combining fibre arrays and perovskite nanocrystals, we have experimentally demonstrated a threefold increase in output signal and achieved 6-MeV and 10-MeV gamma-ray imaging via a 4-mm-thick scintillator layer. Gamma-ray imaging is important for measuring skin doses during radiotherapy, medical diagnostics and industrial 3D gamma-ray tomography, which requires a deep penetration depth[42,43]. In addition to photon detectors, the hemispherical detector and the fibre array reported herein also have application potential for compound eye bionics and light-field imaging[44,45]. Considering the compatibility with silicon technology and the stretchability of the material, these double-tapered fibre arrays could be used for mass production of ultrasensitive photon detectors and large-area flexible imaging devices for high-energy radiation. Future research directions beyond radiation detection and imaging include biomolecule sensing, optical amplifiers and light-emitting diodes, among others. A biologically inspired system, such as adding hydrophobic structures to fibre surfaces to adapt to different applications, is also of interest.

Online content

Any methods, additional references, Nature Portfolio reporting summaries, source data, extended data, supplementary information, acknowledgements, peer review information; details of author contributions and competing interests; and statements of data and code availability are available at https://doi.org/10.1038/s41566-023-01204-1.

References

1. Yakunin, S. et al. Detection of gamma photons using solution-grown single crystals of hybrid lead halide perovskites. *Nat. Photon.* **10**, 585–589 (2016).
2. Cao, Z. et al. Ultrahigh-energy photons up to 1.4 petaelectronvolts from 12 γ-ray galactic sources. *Nature* **594**, 33–36 (2021).
3. Kataoka, J. et al. Recent progress of MPPC-based scintillation detectors in high precision X-ray and γ-ray imaging. *Nucl. Instrum. Methods Phys. Res. A* **784**, 248–254 (2015).
4. Franks, L. et al. *Hard X-Ray, Gamma-Ray and Neutron Detector Physics XVII* Vol. 9593 (SPIE, 2015).
5. Oshima, T. et al. Development of a high-precision color γ-ray image sensor based on TSV-MPPC and diced scintillator arrays. *Nucl. Instrum. Methods Phys. Res. A* **803**, 8–14 (2015).
6. Roques-Carmes, C. et al. A framework for scintillation in nanophotonics. *Science* **375**, eabm9293 (2022).
7. Kim, Y. C. et al. Printable organometallic perovskite enables large-area, low-dose X-ray imaging. *Nature* **550**, 87–91 (2017).
8. Zhao, J. et al. Perovskite-filled membranes for flexible and large-area direct-conversion X-ray detector arrays. *Nat. Photon.* **14**, 612–617 (2020).
9. Gao, Y. et al. Ultrathin and ultrasensitive direct X-ray detector based on heterojunction phototransistors. *Adv. Mater.* **33**, e2101717 (2021).
10. Zhuang, R. et al. Highly sensitive X-ray detector made of layered perovskite-like (NH4)$_3$Bi$_2$I$_9$ single crystal with anisotropic response. *Nat. Photon.* **13**, 602–608 (2019).
11. Heo, J. H. et al. High-performance next-generation perovskite nanocrystal scintillator for nondestructive X-ray imaging. *Adv. Mater.* **30**, e1801743 (2018).
12. Pan, W. et al. Cs$_2$AgBiBr$_6$ single-crystal X-ray detectors with a low detection limit. *Nat. Photon.* **11**, 726–732 (2017).
13. Shrestha, S. et al. High-performance direct conversion X-ray detectors based on sintered hybrid lead triiodide perovskite wafers. *Nat. Photon.* **11**, 436–440 (2017).
14. Wei, H. et al. Sensitive X-ray detectors made of methylammonium lead tribromide perovskite single crystals. *Nat. Photon.* **10**, 333–339 (2016).
15. Deumel, S. et al. High-sensitivity high-resolution X-ray imaging with soft-sintered metal halide perovskites. *Nat. Electron.* **4**, 681–688 (2021).
16. Wei, H. et al. Dopant compensation in alloyed CH$_3$NH$_3$PbBr$_{3-x}$Cl$_x$ perovskite single crystals for γ-ray spectroscopy. *Nat. Mater.* **16**, 826–833 (2017).
17. He, Y. et al. CsPbBr$_3$ perovskite detectors with 1.4% energy resolution for high-energy γ-rays. *Nat. Photon.* **15**, 36–42 (2020).
18. He, Y. et al. High spectral resolution of γ-rays at room temperature by perovskite CsPbBr$_3$ single crystals. *Nat. Commun.* **9**, 1609 (2018).
19. Chen, Q. et al. All-inorganic perovskite nanocrystal scintillators. *Nature* **561**, 88–93 (2018).
20. Büchele, P. et al. X-ray imaging with scintillator-sensitized hybrid organic photodetectors. *Nat. Photon.* **9**, 843–848 (2015).
21. Basirico, L. et al. Direct X-ray photoconversion in flexible organic thin film devices operated below 1V. *Nat. Commun.* **7**, 13063 (2016).
22. Ciavatti, A. et al. Toward low-voltage and bendable X-ray direct detectors based on organic semiconducting single crystals. *Adv. Mater.* **27**, 7213–7220 (2015).
23. Liu, X. et al. Solution-grown formamidinium hybrid perovskite (FAPbBr$_3$) single crystals for α-particle and γ-ray detection at room temperature. *ACS Appl. Mater. Interfaces* **13**, 15383–15390 (2021).
24. Mills, C. A. et al. Direct detection of 6-MV X-rays from a medical linear accelerator using a semiconducting polymer diode. *Phys. Med. Biol.* **58**, 4471–4482 (2013).
25. Loke, G. et al. Digital electronics in fibres enable fabric-based machine-learning inference. *Nat. Commun.* **12**, 3317 (2021).
26. Brodnik, G. M. et al. Optically synchronized fibre links using spectrally pure chip-scale lasers. *Nat. Photon.* **15**, 588–593 (2021).
27. Kanik, M. et al. Strain-programmable fiber-based artificial muscle. *Science* **365**, 145–150 (2019).
28. Rein, M. et al. Diode fibres for fabric-based optical communications. *Nature* **560**, 214–218 (2018).
29. Canales, A. et al. Multifunctional fibers for simultaneous optical, electrical and chemical interrogation of neural circuits in vivo. *Nat. Biotechnol.* **33**, 277–284 (2015).
30. Korposh, S. et al. Tapered optical fibre sensors: current trends and future perspectives. *Sensors* **19**, 2294 (2019).
31. Stranks, S. D. et al. The physics of light emission in halide perovskite devices. *Adv. Mater.* **31**, e1803336 (2019).
32. Cho, C. et al. The role of photon recycling in perovskite light-emitting diodes. *Nat. Commun.* **11**, 611 (2020).
33. Pisano, F. et al. Depth-resolved fiber photometry with a single tapered optical fiber implant. *Nat. Methods* **16**, 1185–1192 (2019).
34. Pisanello, F. et al. Dynamic illumination of spatially restricted or large brain volumes via a single tapered optical fiber. *Nat. Neurosci.* **20**, 1180–1188 (2017).
35. Pazos-Outón, L. M. et al. Photon recycling in lead iodide perovskite solar cells. *Science* **351**, 1430–1433 (2016).
36. Dong, Q. et al. Electron-hole diffusion lengths > 175 µm in solution-grown CH$_3$NH$_3$PbI$_3$ single crystals. *Science* **347**, 967–970 (2015).
37. Fassl, P. et al. Revealing the internal luminescence quantum efficiency of perovskite films via accurate quantification of photon recycling. *Matter* **4**, 1391–1412 (2021).
38. Richter, J. M. et al. Enhancing photoluminescence yields in lead halide perovskites by photon recycling and light out-coupling. *Nat. Commun.* **7**, 13941 (2016).
39. Yu, H., Chen, T., Han, Z., Fan, J. & Pei, Q. Liquid scintillators loaded with up to 40 weight percent cesium lead bromide quantum dots for gamma scintillation. *ACS Appl. Nano Mater.* **5**, 14572–14581 (2022).
40. Pan, L., Shrestha, S., Taylor, N., Nie, W. & Cao, L. R. Determination of X-ray detection limit and applications in perovskite X-ray detectors. *Nat. Commun.* **12**, 5258 (2021).
41. Zaffalon, M. L. et al. Extreme γ-ray radiation hardness and high scintillation yield in perovskite nanocrystals. *Nat. Photon.* **16**, 860–868 (2022).
42. Adams, R. & Zboray, R. Gamma radiography and tomography with a CCD camera and Co-60 source. *Appl. Radiat. Isot.* **127**, 82–86 (2017).
43. Jones, E. A., Phan, T. D., Blanchard, D. A. & Miley, A. Breast-specific γ-imaging: molecular imaging of the breast using ^{99m}Tc-sestamibi and a small-field-of-view γ-camera. *J. Nucl. Med. Technol.* **37**, 201–205 (2009).
44. Gu, L. et al. A biomimetic eye with a hemispherical perovskite nanowire array retina. *Nature* **581**, 278–282 (2020).
45. Song, Y. M. et al. Digital cameras with designs inspired by the arthropod eye. *Nature* **497**, 95–99 (2013).

Methods

Materials and characterization

CsPbX$_3$ (X = Cl, Br or I) perovskite nanocrystals were synthesized according to a method described in the literature[19]. These nanocrystals were synthesized using a modified hot-injection method after the caesium oleate was synthesized as a caesium precursor. After obtaining perovskite nanocrystals, we dispersed them in a toluene solution of ammonium fluorosilicate. The ammonium fluorosilicate was then hydrolysed to SiO$_2$. As a result of this, the perovskite nanocrystals are protected by SiO$_2$ shells and do not aggregate and degrade back to the bulk phase. Caesium carbonate (Cs$_2$CO$_3$, 99.9%), lead(II) chloride (PbCl$_2$, 99.99%), lead(II) bromide (PbBr$_2$, 99.99%), lead(II) iodide (PbI$_2$, 99.99%), oleylamine (technical grade 70%) and cyclohexane (chromatography grade 99.9%) were purchased from Sigma-Aldrich. A SYLGARD™ 184 silicone elastomer kit and epoxy resin were purchased from Dow Corning.

Photoluminescence and absorption spectra were recorded using an Edinburgh FS5 fluorescence spectrophotometer (Edinburgh Instruments) equipped with a miniature X-ray source (AMPEK). Radioluminescence spectra were measured using a fibre-coupled fluorescence spectrometer (Ocean Optics QE PRO).

Refractive index of the perovskite used for optical simulations

We determined the complex refractive index $\mathbf{n}(\omega) = n(\omega) + \mathbf{i}\kappa(\omega)$ of the perovskites according to the Kramers–Kronig (KK) relations. First, we obtained $\kappa(\omega)$ from the excitation spectrum ($E(\omega)$) by assuming that the measured absorption is proportional to the film absorption:

$$E(\omega) = P_0 \times \{1 - \log[-\alpha(\omega) \times d]\} \tag{1}$$

$$\kappa(\omega) = \frac{c \times \alpha(\omega)}{2\omega} = -\frac{c \exp(1 - E(\omega)/P_0)}{2\omega d} \tag{2}$$

where c is the speed of light in vacuum and ω is the angular frequency of the light.

The $n(\omega)$ can then be obtained from $\kappa(\omega)$ according to the KK relations. For convenience, we use a subtractive KK analysis, defined by[46]

$$n(\omega) = n(\omega_0) + \frac{2}{\pi}(\omega^2 - \omega_0^2)P\int_0^\infty \frac{\omega'\kappa(\omega')}{(\omega^2 - \omega'^2)(\omega_0^2 - \omega'^2)}\,d\omega' \tag{3}$$

where $n(\omega_0)$ is the refractive index measured at the reference frequency ω_0 to provide scaling of the calculated curves, and P is the Cauchy principal value of the integral. Thus, knowledge of the absorption spectrum in combination with a measurement at a reference frequency allows the refractive index spectrum to be determined. We use the interference method to determine the refractive index of the perovskite film at 532 nm as 1.81 and obtain the complex refractive index using equations (1)–(3).

Simulation of photon recycling

A Monte Carlo simulation was used to analyse external emission spectra in the perovskite films, taking into account both photon recycling and scattering effects. The initial isotropic photoluminescence is generated after local photoexcitation. Emitted isotropic photons with an emission angle within the escape cone escape from the film surfaces. As the photons exit the escape cone, they are either reabsorbed and re-emitted isotropically, or they are trapped within the film and propagate via total internal reflection before being scattered.

In applying the Monte Carlo program, the following input parameters are required: the number of initially absorbed photons n, the internal quantum efficiency QE$_i$ of the perovskite, the escape-cone probability p_{ed} of the film, the film thickness d, the scattering coefficient l_s, the absorption spectrum $\alpha(\lambda)$ and the internal emission spectra $E_i(\lambda)$. The program then differentiates the number of photons initially absorbed (n_{abs}) into four contributions: reabsorption (n_{abs-PR}), direct

escape (n_{esc-d}), scattering and escape (n_{esc-s}) and loss due to non-radiative recombination. These quantities allow calculation of the external quantum efficiency and the external emission spectrum of the perovskite film.

The simulation steps are briefly summarized as follows:

(1) Absorbed photons either emit with probability QE$_i$ and the internal photoluminescence spectrum $E_i(\lambda)$ or are lost non-radiatively with probability $(1 - \text{QE}_i)$.

(2) Emitted photons either escape the film with probability $p_{ed}(\lambda)$ and are reabsorbed with probability $(p_{ed} - p_{ed}(\lambda))$ following Beer–Lambert's law, or they are trapped in the film with probability $(1 - p_{ed})$.

(3) Trapped photons are either reabsorbed in the film with probability $\alpha(\lambda)/(\alpha(\lambda) + l_s^{-1})$ or scattered out with probability $l_s^{-1}/(\alpha(\lambda) + l_s^{-1})$.

(4) The reabsorbed photons repeat steps 1–3 until all emitted photons have escaped the film either by direct emission or scattering, or non-radiative means.

Experimental investigation of photon recycling in perovskites

Using CsPbBr$_3$ nanocrystals with emission at 520 nm, we coated a 100-μm-thick PDMS substrate with a 20-μm-thick perovskite film. The PDMS substrate was fabricated in a Petri dish using a premixed PDMS prepolymer and a curing agent (10:1 by mass) under vacuum conditions, followed by a 2-h heat treatment at 80 °C. The PDMS replica was separated carefully from the Petri dish. Finally, perovskite nanocrystals dispersed in cyclohexane were coated onto the PDMS substrate.

We measured the spatially resolved photoluminescence using a homemade measurement system. An infinity-corrected ×20 objective (Olympus, NA = 0.4) was used to focus the excitation laser on the sample. The photoluminescence was collected using a ×10 objective (Olympus, NA = 0.3) and focused on the entrance slit of a fibre spectrometer (Ocean Optics). The collection objective and fibre were mounted on a motorized stage to control the distance between the collection and excitation points.

To demonstrate the existence of photon recycling in synthesized perovskite nanocrystals and to analyse its promoting effect on light extraction efficiency, we created a gap in the perovskite film by mechanically removing the region at distances between ~180 μm and 250 μm from the excitation point (O). Signal A observed in the perovskite-free region shows a purely scattered signal, with a peak redshifted by 8 nm from the original signal O at 0 μm. On the other hand, signal B in the perovskite-covered region after the gap shows a relatively broad spectrum and a small redshift because of the coexistence of purely scattered and re-emitted signals. These experimental phenomena demonstrate photon recycling, and the re-emitted light can be re-extracted from the scintillator layer (Supplementary Fig. 6).

Optical analysis of the escape-cone angle from the perovskite layer to optical fibres

The refractive indices of the fibre core, fibre cladding and perovskite layers are n_1, n_2 and n_3, respectively. The incidence and refraction angles of the photoluminescence beam at the interface of the perovskite and cladding are θ_3 and θ_2, respectively, and the refraction angle in the core is θ_1. According to the principles of geometric optics, for light in the cladding that escapes the perovskite layer, the incident angle θ_2 at the interface between the fibre cladding and the fibre core must satisfy

$$\sin\theta_2 > (n_1/n_2)\sin\varphi_c \tag{4}$$

to propagate through total internal reflection after entering the core. φ_c is Brewster's angle and is given by

$$\sin\varphi_c = n_2/n_1 \tag{5}$$

From equations (4) and (5) we can obtain $\sin\theta_2 > 1$, but this inequality cannot hold. Therefore, for a cylindrical optical fibre whose cross-sectional area (S_i) at the incident end is equal to that (S_e) at the exit end, light entering the fibre from the side cannot propagate by total internal reflection.

For a negatively tapered optical fibre ($S_i > S_e$), the incident angle of light in the perovskite layer must satisfy

$$\sin\theta_3 > \frac{n_1}{n_3}\sin(\varphi_c + 2\alpha) > \frac{n_1}{n_3}\sin\varphi_c = \frac{n_2}{n_3} \qquad (6)$$

to enter the fibre core and propagate through total internal reflection, where α is the cone angle. However, light with an incident angle of θ_3 that satisfies equation (6) is totally reflected at the interface between the perovskite layer and the cladding and is therefore unable to enter the fibre core.

For a positively tapered optical fibre ($S_i > S_e$) as used here, the incident angle of light in the perovskite layer must satisfy

$$\frac{n_2}{n_3} > \sin\theta_3 > \frac{n_1}{n_3}\sin(\varphi_c - 2\alpha) \qquad (7)$$

to enter the fibre core and propagate through total internal reflection.

In our design, n_1, n_2 and n_3 are 1.52, 1.41 and 1.82, respectively. Therefore, light with an incident angle of θ_3 between 42.55° and 50.78° can be collected by the fibre from the perovskite layer. This angle defines an escape cone with a solid angle Ω_{esc} with respect to the surface of the perovskite layer. Because spontaneous emission is distributed isotropically over the 4π solid angle, the probability for emitted photons to escape into the fibre and propagate through total internal reflection is

$$\eta_{esc} = \frac{\Omega_{esc}}{4\pi} = \frac{2\pi(\cos 42.55° - \cos 50.78°)}{4\pi} = 5.2\% \qquad (8)$$

Analytical calculation of the light-collection field

To understand the properties of a tapered optical fibre, we first analysed the light-collection field using geometrical optics. There are two factors that determine the collection efficiency: (1) the fraction of photons that reach the entrance pupil and (2) the fraction of these photons that are actually accepted by the fibre system. The first factor is given by the solid angle Ω_e of the entrance pupil of the fibre with respect to the position of the luminescence source. The second factor depends on the maximum acceptance angle Ω_a of the fibre, which is related to its NA, as well as on the source position. In the following, we calculate the collection field at the fibre side and fibre facet separately.

For light collection from the fibre side, Ω_e is calculated by

$$\Omega_e = 2\pi[1 - \cos(\theta_3 - \theta_4)] \qquad (9)$$

where θ_3 and θ_4 are the included angles between the line (connecting the light source and the two ends of the side surface) and the perpendicular line from the light source to the side surface, respectively. They are calculated as

$$\theta_3 = abs(\arctan(\frac{z}{x}) - \alpha) \qquad (10)$$

and

$$\theta_4 = \begin{cases} \alpha + \arctan\left(\frac{H-z}{x+H\tan(\alpha)}\right) & z \leq H + \tan\alpha(x + H\tan\alpha) \\ \arctan\left(\frac{z-H}{x+H\tan(\alpha)}\right) - \alpha & z > H + \tan\alpha(x + H\tan\alpha) \end{cases} \qquad (11)$$

where α and H are the taper angle and the height of the fibre, respectively, and x and z are the spatial position coordinates of the light source.

Ω_a is calculated by

$$\Omega_a = 2\pi[1 - \cos(\theta_2 - \theta_1)] \qquad (12)$$

where θ_1 and θ_2 are the minimum and maximum incident angles at which light can enter the tapered fibre and propagate with total internal reflection, depending on the NA of the fibre and the refractive index of the luminescent layer. They can be expressed as:

$$\theta_1 = \arcsin\left\{\frac{n_1}{n_3}\sin\left[\arcsin\left(\frac{n_2}{n_1}\right) - 2\alpha\right]\right\} \qquad (13)$$

and

$$\theta_2 = \arcsin\left(\frac{n_2}{n_3}\right) \qquad (14)$$

where n_1, n_2 and n_3 are the refractive indices of the fibre core, fibre cladding and luminescent layer, respectively.

The collection efficiency depends on the intersection of the two solid angles of Ω_e and Ω_a. Since the light source emits isotropically, the collection efficiency η_s on the fibre side can be expressed as

$$\eta_s = \frac{\text{Intersection}(\Omega_e, \Omega_a)}{4\pi} \qquad (15)$$

For the light collection from the fibre facet, θ_1, θ_2, θ_3 and θ_4 are calculated as

$$\theta_1 = \arcsin\left\{\frac{n_3}{n_1}\sin\left[90° + \alpha - \arcsin\left(\frac{n_2}{n_1}\right)\right]\right\} \qquad (16)$$

$$\theta_2 = \arcsin\left(\frac{n_2}{n_3}\right) \qquad (17)$$

$$\theta_3 = \arctan\left(\frac{x + H\tan\alpha}{z - H}\right) \qquad (18)$$

and

$$\theta_4 = \arctan\left(\frac{x + H\tan\alpha + b}{z - H}\right) \qquad (19)$$

where b is the fibre core diameter.

Similarly, the collection efficiency η_t at the fibre facet can be calculated by substituting equations (16) to (19) into equations (9), (12) and (15).

Calculation of light-extraction efficiency by integrating recursive photon recycling

The light-extraction efficiency of the optical fibre from the perovskite layer can be calculated by integrating recursive photon recycling processes. We can then derive an expression for the external photoluminescence efficiency η_{ext} by writing it as a series over multiple reabsorption events:

$$\eta_{ext} = \eta_{esc}\eta + (1 - \eta_{esc})\eta^2\eta_{esc} + (1 - \eta_{esc})\eta^3\eta_{esc} + \cdots$$
$$= \eta_{esc}\eta \sum_{k=0}^{\infty} (1 - \eta_{esc})^k\eta^k = \frac{\eta_{esc}\eta}{1 - \eta + \eta_{esc}\eta} \qquad (20)$$

where η is the internal photoluminescence efficiency. In our design, $\eta_{esc} = 5.2\%$. When the internal quantum efficiency η of the perovskite is 80–95%, the external quantum efficiency η_{ext} is 17.2–49.7%. It should be noted that this is the most conservative estimate for light-extraction efficiency. Because $\eta_{esc} = 5.2\%$ is calculated based on geometric optics,

the promotion effect of the tapered structure between the fibres is not considered.

Selection of fibre filling ratio and film thickness

Light transmittance under specific fibre parameters is related to the film thickness and the fibre fill factor of scintillator films with tapered optical fibres (Supplementary Fig. 4). For example, when the fibre taper angle is constant, a thicker film can fill fewer fibres for X-rays with an attenuation coefficient of 10 cm⁻¹. Although a 400-μm film absorbs more X-rays than its 300-μm counterpart, the former has a lower light-collection efficiency because the latter can be filled with more tapered fibres. As the film thickness is reduced to 100 μm, additional optical fibres can be accommodated. However, as the fibre fill rate continues to increase, scintillators cannot absorb sufficient X-rays, resulting in reduced light output. As a result, for X-rays with a certain energy, there is an optimal scintillator film design with embedded optical fibres, and spatial resolution must also be considered.

Device manufacturing

We fabricated double-tapered fibre arrays by moulding and laminating polyurethane and silicone elastomers. First, the mould of fibre arrays was produced by high-precision 3D printing with a resolution of 2 μm (Micro-Arch S130, Mofang Technology Co.). The 3D mould template was sufficiently washed with heptane and left in the oven at 60 °C for 6 h to remove any residual that might affect silicone curing. Then, parts A and B of Dragon Skin 20 were mixed at a 1:1 ratio and mixed in a planetary centrifugal mixer at 200 r.p.m. for 5 min. The prepolymer was poured into the 3D-printed mould and cured at 60 °C in an oven for 1 h. The cured silicone was demoulded and placed on a flat surface with the cavity side facing up. The fibre array was made of a transparent epoxy resin (EA E-30CL, Loctite Chemical Co.). Parts A and B of EA E-30CL were mixed at a 3:1 ratio and mixed in a planetary centrifugal mixer at 2,000 r.p.m. (448g) for 1 min. The epoxy resin was poured into the silicone and cured at room temperature for 16 h. After curing, the mould was released to obtain the microneedle array of epoxy resin. The microneedle array was immersed in PDMS diluted with cyclohexane (SYLGARD™ 184 silicone elastomer kit, Dow Corning; parts A and B are mixed at a 10:1 ratio) and then placed in an oven for curing to complete the cladding process. After these processes, the fibre array was obtained, and luminescent materials such as perovskite nanocrystals could be added. The key points for fabrication are as follows: (1) all materials need to be mixed evenly before curing; (2) for the demoulding process, sufficient cooling is needed to relieve the stress formed during material solidification; and (3) minor defects on the fibre surface must be repaired by dipping.

The fabrication process of the hemisphere detector is similar to the process described above, except that a flexible polyurethane elastomer (Clear Flex™ 30) was used for fabrication of the fibre arrays. After the fibre arrays were processed, the cyclohexane was added to swell them into a hemisphere, and a transparent hemisphere was used as the support. Scintillators were then added onto the fibre substrate and cured.

X-ray detection and imaging

For X-ray imaging, a mini X-ray tube (P_{max} = 4 W, V_{max} = 50 kV, I_{max} = 79 μA) from Amptek was utilized as the X-ray source. The X-ray dose rate was altered by adjusting the current of the X-ray tube from 5 μA to 79 μA. Imaging objects and scintillator wafers were placed vertically in relation to the incident X-rays, and the scintillators were fixed directly behind the objects. A reflector was used to deflect the optical path by 90° and reduce the negative influence of the direct radiation from the X-ray source on the camera. Photographs of X-ray-induced radioluminescence were acquired with a digital camera (Canon; lens EF 100 f/2.8 L IS USM).

Gamma-ray detection and imaging

The gamma-ray imaging system is similar to the X-ray imaging system. The gamma-ray source used is a radiotherapy system from National Cancer Centre Singapore (TrueBeam, Varian Medical Systems), which uses a tungsten anode and 6-MV or 10-MV accelerating voltages. The spot size and rotation direction of the gamma rays can be adjusted. The scintillator film was placed vertically in relation to the incident gamma rays, and a reflector was used to deflect the optical path by 90°. The scintillation of the gamma rays was detected using a fibre-optic spectrometer and images were taken using a smartphone or a digital camera (Canon, lens EF 100 f/2.8 L IS USM).

MTF measurements

The spatial resolution can be determined by the value of the spatial frequency when the MTF is equal to 0.2. We use the X-ray source to image an aluminium plate patterned with different line pairs of different spatial frequencies by placing it on a scintillator film. The MTF is calculated by finding the contrast between the maximum brightness I_{max} and the minimum brightness I_{min} in the line pair. The calculation formula is:

$$\text{MTF} = \frac{I_{max} - I_{min}}{I_{max} + I_{min}} \tag{21}$$

We calculated and plotted MTF values at many different spatial frequencies. The spatial frequency at MTF = 0.2 is the image resolution of our imaging system.

Detection limit calculation

The detection limits for X-rays and gamma rays were calculated by measuring the dark nose signal and sensitivity derived from the slope of fitting lines. The specific calculation formula is:

$$\sigma_{I_{dark}} = \sqrt{\frac{1}{N} \sum_i^N (I_i - \bar{I}_{dark})^2} \; (N = 500)$$
$$I_{lim} = 3.29\sigma_{I_{dark}} \tag{22}$$
$$D_{lim} = I_{lim}/A$$

where N is the number of acquisition points of the dark noise signal acquired without X-ray irradiation, and A is the sensitivity of the linear fit. The calculation results are as follows: for 50-keV X-rays, $\sigma_{I_{dark}}$ = 255.2481, I_{lim} = 839.766 and D_{lim} = 3.5 nGy; for 10-MeV gamma rays, $\sigma_{I_{dark}}$ = 702.9214, I_{lim} = 2,312.61 and D_{lim} = 21.8 μGy.

Gamma pulse height analysis

A Cs-137 source (662-keV characteristic gamma energy) was used, and the sample was placed in a sample holder coupled to an R6231 photomultiplier tube (spectral response peak at 420 nm) using silicone oil. The acquisition time was set to ~1 h. The signal was read out using a BH-132 multichannel analyser with 1,024 channels.

Light yield calculation

To quantify the light yield (LY), we selected a commercial Gd_2O_2S (GOS) scintillator as a reference, for which the light yield is 62,000 photons MeV⁻¹. First, the X-ray attenuation efficiencies of $CsPbBr_3$ and Gd_2O_2S were calculated based on the chemical formula and crystal density, then the spectral data of the two samples under X-ray irradiation (50 kV, 79 μA) were obtained. By comparing the integrated intensities of the two spectra, the light yield of $CsPbBr_3$ can be calculated as follows:

$$\text{LY}_{CsPbBr_3} = \frac{I_2}{b} / \frac{a}{I_1} \cdot \text{LY}_{GOS} \tag{23}$$

where I_1 and I_2 are the radioluminescence intensities of the GOS film and the fibre-containing $CsPbBr_3$ film, and a and b are the X-ray attenuation efficiencies of the GOS film and the fibre-containing $CsPbBr_3$ film.

Data availability
The data that support the findings of this study are available from the corresponding authors upon reasonable request.

Code availability
The codes are available from the corresponding authors upon reasonable request.

References

46. Faber, D. J. et al. Oxygen saturation-dependent absorption and scattering of blood. *Phys. Rev. Lett.* **93**, 028102 (2004).

Author contributions
L.Y., B.H. and X.L. conceived and designed the project. X.L. supervised the project. H.Z. characterized the materials. L.Y. conducted the numerical simulations. B.H. performed device fabrication. B.H., L.Y. and H.Q.T. performed gamma-ray experiments. L.Y. and B.H. wrote the manuscript. X.L. edited the manuscript. All authors participated in the discussion and analysis of the manuscript.

Competing interests
The authors declare no competing interests.

Additional information
Supplementary information The online version contains supplementary material available at https://doi.org/10.1038/s41566-023-01204-1.

Correspondence and requests for materials should be addressed to Xiaogang Liu.

Peer review information *Nature Photonics* thanks Jiang Tang and the other, anonymous, reviewer(s) for their contribution to the peer review of this work.

Reprints and permissions information is available at www.nature.com/reprints.